Supplementary Materials for

TiO_2-coated rutile oxide catalysts for acidic oxygen evolution: A design principle

Georgios K. Stavroglou, Adrian M. Frandsen, Henrik H. Kristoffersen, Katrine L. Svane and Jan Rossmeisl*

*Corresponding author. Email: Jan.Rossmeisl@chem.ku.dk

Section S1: Reaction pathways

Fig. S1 illustrates the reaction intermediates and pathways that were considered for OER in the present work. The equations for the AEM pathway are given in the main text, while the corresponding equations for the alternative pathways are:

$$* + H_2O(l) \rightarrow {}^*O + Hb + H^+ + e^- \quad \text{(S1)}$$

$$\Delta G_1 = \Delta G_{*\mathrm{O+Hb}} - eU_{\mathrm{RHE}}$$

$${}^*O + Hb \rightarrow {}^*O + H^+ + e^- \quad \text{(S2)}$$

$$\Delta G_2 = \Delta G_{*\mathrm{O}} - \Delta G_{*\mathrm{O+Hb}} - eU_{\mathrm{RHE}}$$

$${}^*O + H_2O(l) \rightarrow {}^*O_2 + Hb + H^+ + e^- \quad \text{(S3)}$$

$$\Delta G_3 = \Delta G_{*\mathrm{O_2+Hb}} - \Delta G_{*\mathrm{O}} - eU_{\mathrm{RHE}}$$

$${}^*O_2 + Hb \rightarrow O_2(g) + H^+ + e^- + * \quad \text{(S4)}$$

$$\Delta G_4 = \Delta G_{O_2} - \Delta G_{*\mathrm{O_2+Hb}} - eU_{\mathrm{RHE}}$$

or

$${}^*O + H_2O(l) \rightarrow O_2(g) + Hb + H^+ + e^- \quad \text{(S5)}$$

$$\Delta G_3 = \Delta G_{O_2} + \Delta G_{\mathrm{Hb}} - \Delta G_{*\mathrm{O}} - eU_{\mathrm{RHE}}$$

$$* + Hb \rightarrow H^+ + e^- + * \quad \text{(S6)}$$

$$\Delta G_4 = -\Delta G_{\mathrm{Hb}} - eU_{\mathrm{RHE}}$$

where Hb is a hydrogen atom adsorbed on a bridge oxygen atom of the surface, that is adjacent to the adsorption site (*). The DFT adsorption energy of an adsorbate (A =*OH, *O + Hb, *O, *O_2 + Hb and Hb) is calculated as:

$$\Delta E_{\mathrm{DFT}} = E_{\mathrm{slab+}} + \frac{n}{2}E_{\mathrm{H_2}} - E_{\mathrm{slab}} - E_{\mathrm{H_2O}} \quad \text{(S7)}$$

where $E_{\mathrm{slab+}}$ is the energy of the slab with the adsorbate, E_{slab} is the energy of the bare slab without the adsorbate, $E_{\mathrm{H_2O}}$, $E_{\mathrm{H_2}}$ are the energies of H_2O and H_2 in the gas phase,

respectively, and n is the number of electrons involved in the reaction. The AEM pathway is limited by the scaling relation between the adsorption energies of the *OH and *OOH intermediates ($\Delta G_{*\mathrm{OOH}} \approx \Delta G_{*\mathrm{OH}} + 3.2$ eV) and therefore requires a minimum potential of 1.6 V.[1] For the pathway that involves the reaction steps of eqn (S1)–(S4), the corresponding energy difference between the *O + Hb and *O_2 + Hb intermediates depend on the element at the adsorption site. For some elements it is therefore possible to have a more favourable minimum potential than for the AEM pathway.[2] Moreover, the formation of O_2(g) during the third step of the OER (eqn S5 and S6) was also considered. The free energy of an oxygen molecule is set to 4.92 eV. This is to avoid calculating the energy of O_2, because it is poorly described by DFT.[3] When calculating the overpotential we assume that the reaction follows the minimum energy pathway, and as a result, a combination of pathways is also possible.

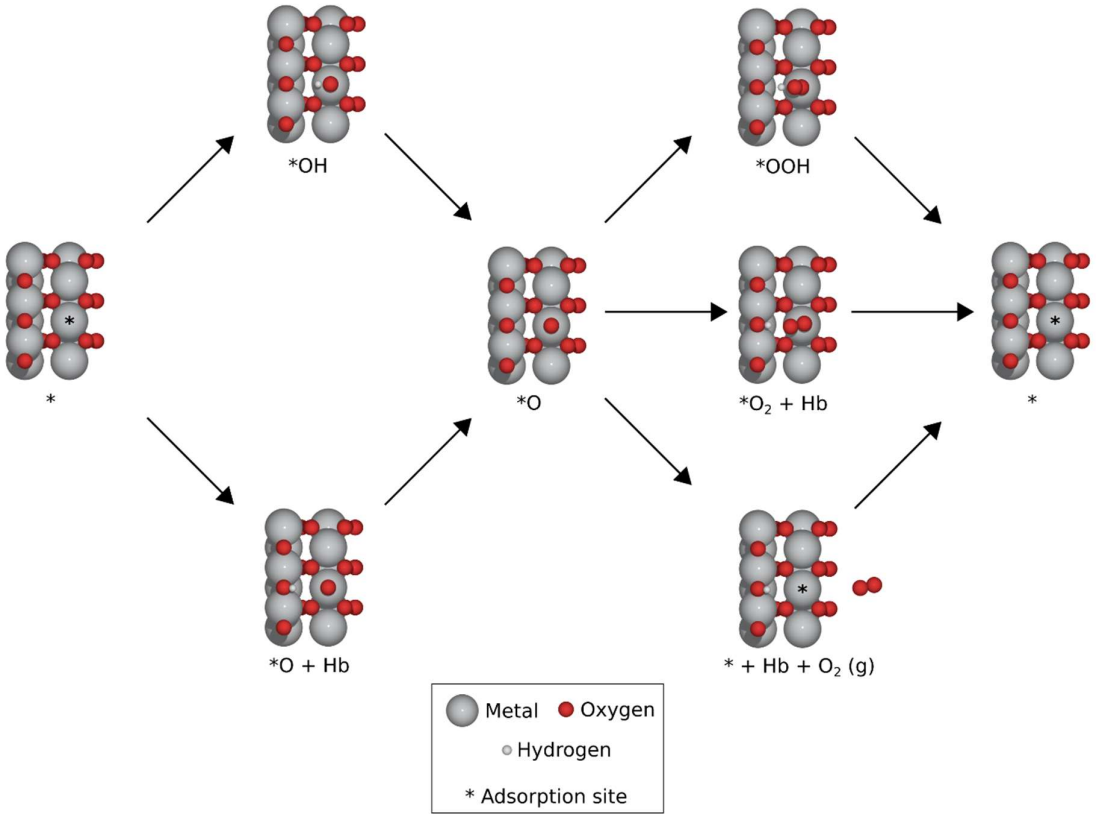

Fig. S1 Possible reaction pathways for the oxygen evolution reaction (OER) on the rutile oxides under study. The cus active site is denoted with an asterisk (*). We assume that the reaction follows the minimum energy pathway, meaning that a combination of pathways is also possible.

Section S2: Calculations setup

All Density Functional Theory (DFT) calculations were performed using the GPAW software package, with The Atomic Simulation Environment (ASE) used to set up and analyse the calculations.[4-6] The exchange and correlation energy is calculated with the RPBE functional,[7] utilizing a plane-wave (PW) basis set with an energy cutoff of 500 eV. We used a (2,2,1) k-point sampling, and the surface was modelled as a 3 × 1 slab of rutile (110). The slabs consists of four MO_2 layers (M = transition metal), with the bottom two layers fixed to their bulk positions For TiO_2-coated oxides with one TiO_2 layer, the top layer of the parent slab was replaced by TiO_2 so that the slab still contained four layers. To consider the effect of two TiO_2 layers, an extra layer is added so that the slabs contain five MO_2 layers in total. For the $W_xPt_{1-x}O_2$ and $W_{0.46}Pd_{0.54}O_2$ compositions, we retained four MO_2 layers and added a single TiO_2 layer as the fifth layer. A dipole correction was used to decouple the electrostatic potentials, and a vacuum region of at least 10 Å was added on either side of the slab. The structures are relaxed until the forces on all atoms are below 0.05 eV $Å^{-1}$. This calculation setup is identical to the one used in ref. 8, such that the generated data is consistent with the employed high entropy oxide data.

Spectator *O species are sometimes present on the undercoordinated sites (cus) neighbouring the active site. In ref. 8, spectator *O species were always adsorbed on neighbouring cus sites, and this is carried over to our use of the dataset. However, in the remaining calculations, we only add spectator *O species to Os, Ru, and Ir cus sites, while keeping other neighbouring cus sites empty. This is because pure OsO_2, RuO_2, and IrO_2 (110) surfaces lie on the strong-binding side of the volcano (ΔG_2 < 1.6 eV), so the OER activity is limited by the conversion of *O to *OOH or $*O_2$ + Hb. Due to the slow conversion of *O, the Os, Ru, and Ir surface sites will, in general, be covered by *O species at OER conditions.

Section S3: RuRhIrOsTi high entropy oxide dataset

The high entropy oxides (HEOs) bare surfaces, *OH, and *O intermediates have been published as part of ref. 8. The HEO slabs consist of an average composition of $Ru_{0.2}Rh_{0.2}Ir_{0.2}Os_{0.2}Ti_{0.2}O_2$ and they are randomly generated. The adsorption energies for each active site element is investigated with a substantial and nearly equal amount of data (Fig. S2). The constituents oxides are conductive, except for TiO_2, offering a conductive HEO and resulting in a structure where charge is readily provided for the OER. Because our conducting oxides have multiple electrons at, or close to, the Fermi level, we avoid the computational challenges associated with doped semiconducting oxides, where electrons are localized at individual dopant sites, and consequently, reactions that require electrons from the surface, e.g. formation of *OH or O*, depend strongly on the type and number of specific dopants present in such system.[9]

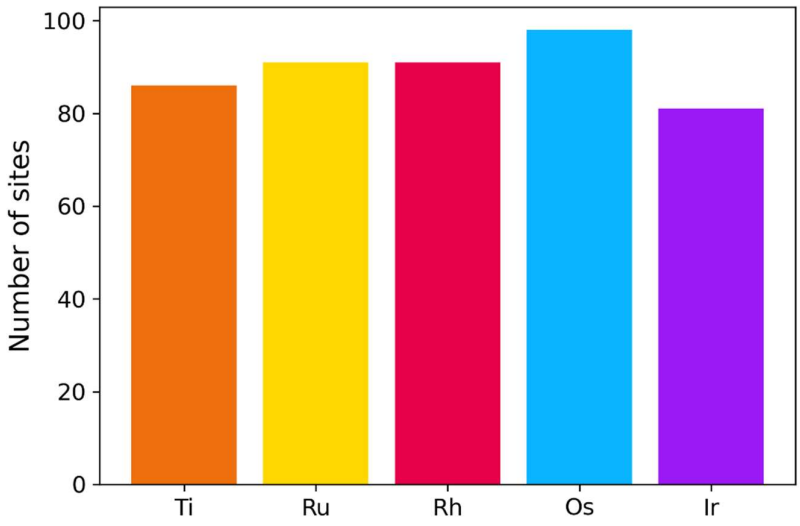

Fig. S2 Number of active sites investigated across Ti, Ru, Rh, Os, and Ir elements of the HEOs data.

Section S4: Description of the model structures

The chemical systems in this study are categorized in four main datasets. Structural and computational specifications for the slab models used in each dataset are summarized in Table S1, with further compositional details provided below.

Table S1 Structural specifications for the slab models used in each one of the four datasets studied in this work. The number of different slabs includes the OER intermediates. Part of the data from the " Host (HEO) – Guest " has been published in ref. 8.

Dataset	**Number of MO_2 layers**	**Number of metal atoms**	**Number of different compositions**	**Number of different slabs**
Host (Pure oxide) – Guest	4	24	72	452
Host (HEO) – Guest	4	24	447	1685
TiO_2-coated metal (Ru, Rh, Ir, Os, Pd, Pt) oxides	4 (including 1 TiO_2)	24 (6 Ti)	78	546
	5 (including 2 TiO_2)	30 (12 Ti)	78	546
TiO_2-coated $W_xPt_{1-x}O_2$ and $W_xPd_{1-x}O_2$	5 (including 1TiO_2)	30 (6 Ti)	12	204
Total			687	3433

Host (Pure oxide)–Guest

This dataset consists of all possible combinations of eight pure oxide hosts (RuO_2, IrO_2, RhO_2, OsO_2, PdO_2, PtO_2, TiO_2, and SnO_2) and nine guest elements (Ru, Rh, Ir, Os, Pd, Pt, Ti, Sn, and Zr) (see examples on Fig. S3). The lattice constants of the bulk structures of the pure rutile oxides in this work are given in Table S2.

Table S2 Lattice constants of the pure rutile oxides

System	a (Å)	c (Å)
IrO_2	4.59	3.19
OsO_2	4.56	3.19
PdO_2	4.67	3.21
PtO_2	4.65	3.23
RhO_2	4.60	3.14
RuO_2	4.57	3.14
SnO_2	4.88	3.22
TiO_2	4.70	2.99
WO_2	4.93	2.66

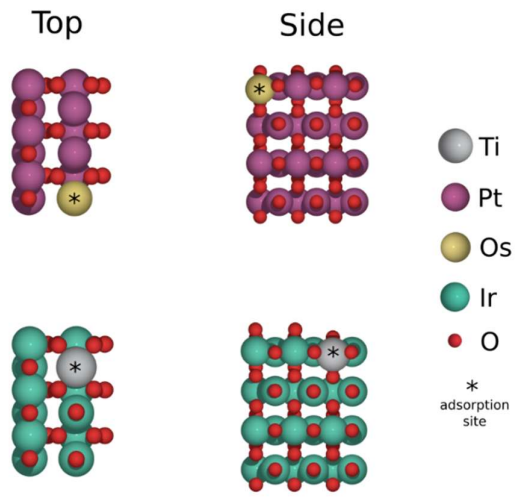

Fig. S3 Optimised slab models for two examples from the Host (Pure oxide)–Guest dataset. The upper panels show an Os guest atom on a PtO_2 host; the lower panels show a Ti guest atom on an IrO_2 host.

Host (HEO)–Guest

This dataset consists of near-equimolar HEOs composed of Ti, Ir, Ru, Rh and Os (see examples on Fig. S4). The bare surfaces and the *OH and *O OER intermediates have been published in ref. 8, totaling 1341 configurations. In our work, we calculated *O+Hb, *O_2+Hb, and O_2(g)+Hb

for all the bare surfaces where Ti is the adsorption site. These calculations added 344 new slabs to the dataset.

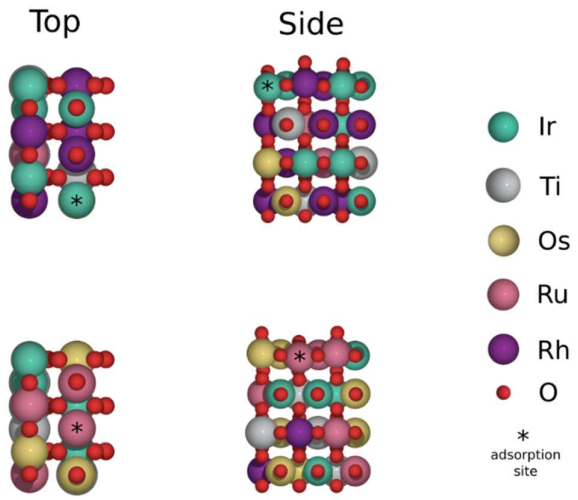

Fig. S4 Optimised slab models for two examples from the Host (HEO)–Guest dataset. The upper panels show an Ir guest atom on a HEO host; the lower panels show a Ru guest atom on a different HEO host.

TiO_2-coated metal (Ru, Rh, Ir, Os, Pd, Pt) oxides

This dataset consists of TiO_2-coated rutile oxides containing Ir, Ru, Os, Rh, Pd, and Pt. We modelled pure RuO_2, RhO_2, IrO_2, OsO_2, PdO_2, and PtO_2 substrates, as well as substrates containing 89%, 78%, and 56% of each oxide, with the remainder being a random mixture of the other five oxides (see examples on Fig. S5). Both one and two TiO_2 coating layers were studied. We examined one of the cus sites as the adsorption site.

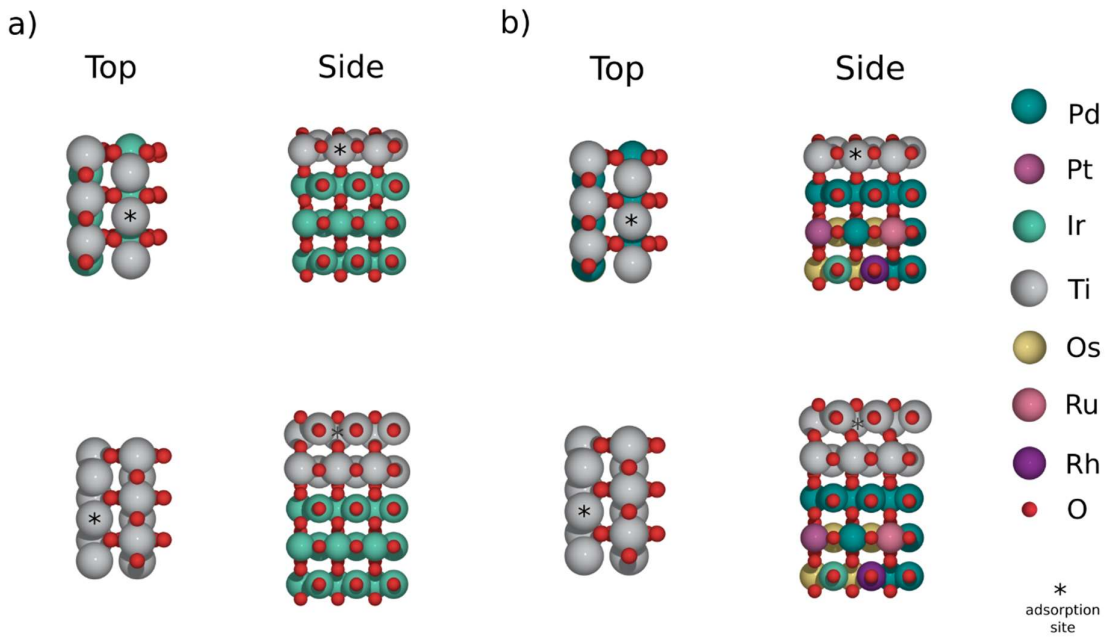

Fig. S5 Optimised slab models from the TiO_2-coated metal oxides (M = Ru, Rh, Ir, Os, Pd, Pt) dataset. Examples show: (a) a pure IrO_2 substrate and (b) a PdO_2 substrate doped with a 44% mixture of Ru, Rh, Ir, Os, and Pt, each coated with one (upper panel) and two (lower panel) TiO_2 layers.

TiO_2-coated $W_xPt_{1-x}O_2$ and $W_{0.46}Pd_{0.54}O_2$

This dataset examines TiO_2-coated rutile binary oxides: $W_xPt_{1-x}O_2$ (x=0.04, 0.08, 0.12, 0.17, 0.21, and 1) and $W_{0.46}Pd_{0.54}O_2$ (see examples on Fig. S6). A single TiO_2 layer has been applied. Two different atomic configurations were studied for each composition. We examined all 3 cus sites as adsorption sites.

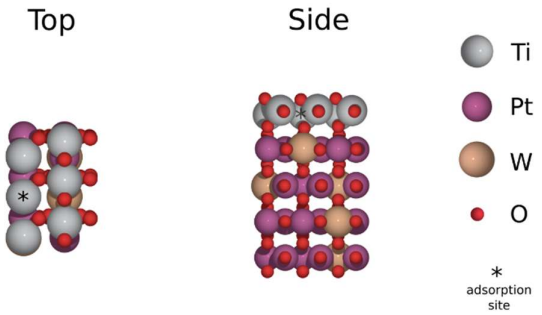

Fig. S6 Top and side view of the optimised slab model for the TiO_2-coated $W_{0.21}Pt_{0.79}O_2$ slab.

Section S5: Fermi level alignment

Fig. S7 shows the total density of states (DOS) together with the summed oxygen-2s projected DOS (O 2s band) for the bare slabs of each pure oxide considered in this study. We calculate the O 2s band centroid, $E_{\mathrm{Center,O2s}}$, by integrating the O 2s band from −25 to −15 eV, where the main, non-interacting part of the oxygen 2s band lies. Above −15 eV only a small amount of O 2s states have weight and there is overlap with O 2p and metal d levels. The Fermi level energies calculated by DFT ($E_{\mathrm{Fermi,DFT}}$) are also marked on Fig. S7. The values of the $E_{\mathrm{Center,O2s}}$, $E_{\mathrm{Fermi,DFT}}$, and the Fermi levels obtained by following the procedure described in the main text (eqn (7)), E_{Fermi}, for the bare slabs of the pure oxides are summarised in Table S3. In the case of SnO_2, there is partial overlap between oxygen and tin (Sn) states, which can affect the quality of the E_{Fermi} for systems where the host composition is SnO_2. However, the observations and insights in this work are not dependent on the trends of pure SnO_2 or systems where SnO_2 constitutes the host oxide.

Most of the oxides considered here are conducting, and the position of the Fermi level is therefore unambiguous. For the semiconducting oxides TiO_2 and SnO_2 the Fermi level is positioned in the middle of the band gap and therefore does not correspond to the energy of the highest energy electron. However, we note that the band gap is underestimated for both of these materials (the band gaps obtained from our DFT-RPBE calculations are 1.5 eV for TiO_2 and 0.9 eV for SnO_2, compared with the experimental values of ≈ 3.0 eV,[10] and ≈ 3.6 eV,[11] respectively).

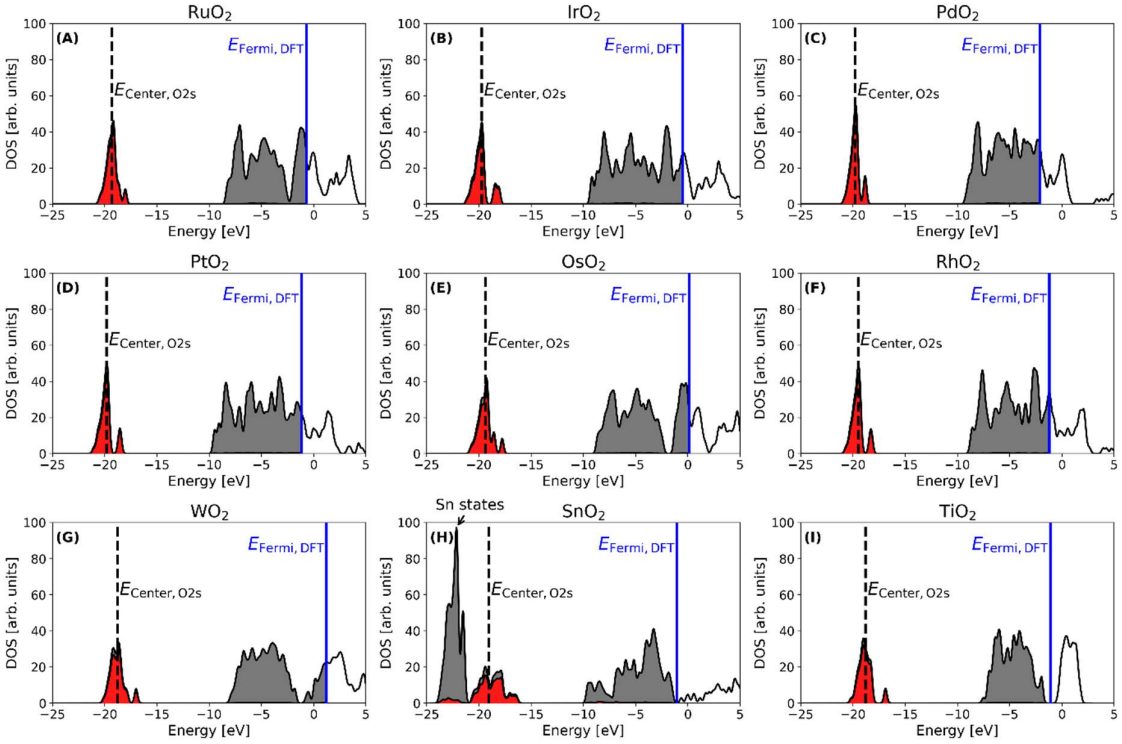

Fig. S7 The total density of states (DOS) (black line) along with the summed oxygen-2s projected DOS (O 2s band, red peak) for the pure oxides IrO_2, OsO_2, PdO_2, PtO_2, RhO_2, RuO_2, WO_2, SnO_2, and TiO_2. The blue vertical line corresponds to the Fermi level calculated by DFT ($E_{Fermi,DFT}$), and the black dashed vertical line corresponds to the centroid of the O 2s band ($E_{Center,O2s}$). States corresponding to Sn in the pure SnO_2 (panel H) are indicated with an arrow. Occupied levels are shaded.

Table S3 Centroid of the oxygen 2s band ($E_{center,O2s}$), Fermi level energy calculated by DFT ($E_{Fermi,DFT}$) and Fermi level energy obtained by following the procedure described in the main text ($E_{Fermi,}$ eqn (7)) of the pure rutile oxides.

Metal oxide	$E_{Center,O2s}$ [eV]	$E_{Fermi,DFT}$ [eV]	E_{Fermi} [eV]
IrO_2	-19.73	-0.48	0.64
OsO_2	-19.39	0.12	0.90
PdO_2	-19.78	-2.09	-0.92
PtO_2	-19.84	-1.17	0.05
RhO_2	-19.52	-1.21	-0.30
RuO_2	-19.30	-0.69	0.00
SnO_2	-19.05	-1.04	-0.59
TiO_2	-18.81	-1.10	-0.90
WO_2	-18.65	1.35	1.39

In Fig. S8, we show the distribution of RPBE band gaps for all systems studied. Most systems are metallic or nearly metallic (band gap ≤ 0.15 eV), with the exception of TiO_2 and SnO_2 hosts, which are semiconducting (Fig. S8f). Because RPBE is known to underestimate band gaps, we also computed non-self-consistent HSE06[12] band gaps for the pure oxides (Table S4). The HSE06 values differ only modestly from RPBE, except for TiO_2 and SnO_2, where the band gaps are significantly larger as expected.

We also compared the E_{Fermi} obtained with RPBE and HSE06 for the TiO_2-coated metal oxides (Ru, Rh, Ir, Os, Pd, Pt) with a single TiO_2 overlayer. As shown in Fig. S9, the HSE06 E_{Fermi} are on average 0.08 eV lower than the RPBE E_{Fermi} values, although there are significant outliers (up to 0.4 eV).

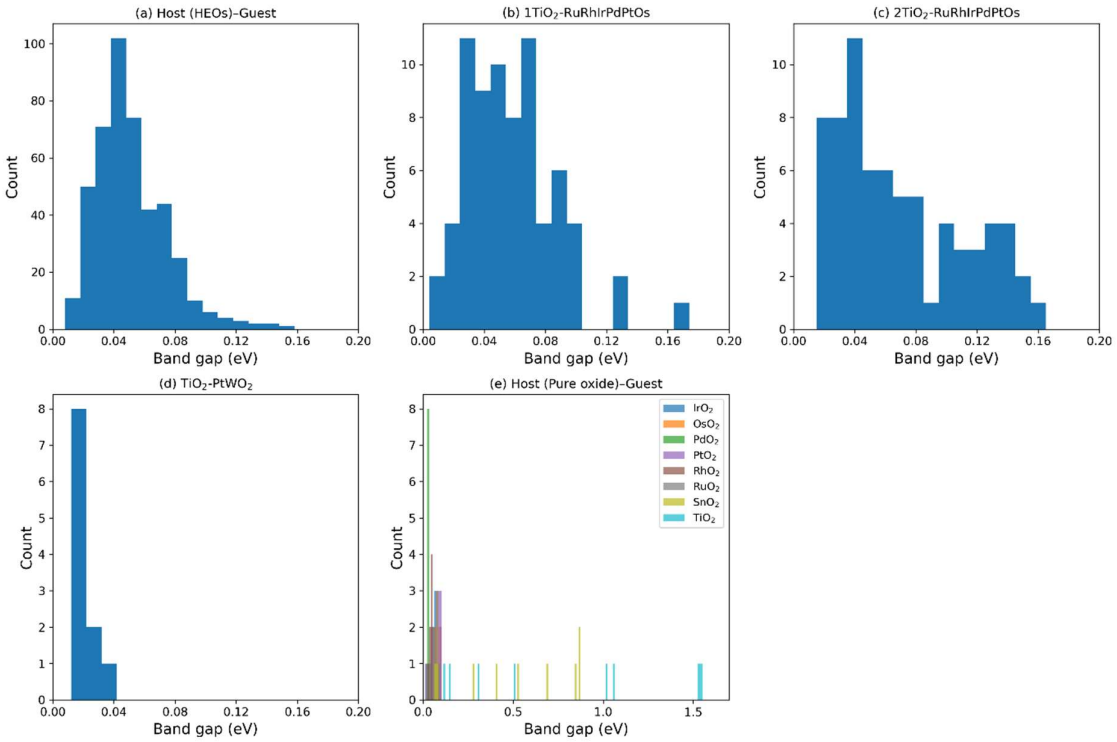

Fig. S8 Band gap distributions for the datasets in our study. The bin size is equal to 0.01 eV.

Table S4 Band gap values calculated with RPBE and HSE06 for the bare surface slabs of the pure oxides.

System	RPBE Band Gap (eV)	HSE06 Band Gap (eV)
IrO_2	0.09	0.23
OsO_2	0.07	0.20
PdO_2	0.03	0.11
PtO_2	0.10	0.16
RhO_2	0.06	0.30
RuO_2	0.04	0.22
SnO_2	0.86	2.14
TiO_2	1.55	3.83
WO_2	0.04	0.13

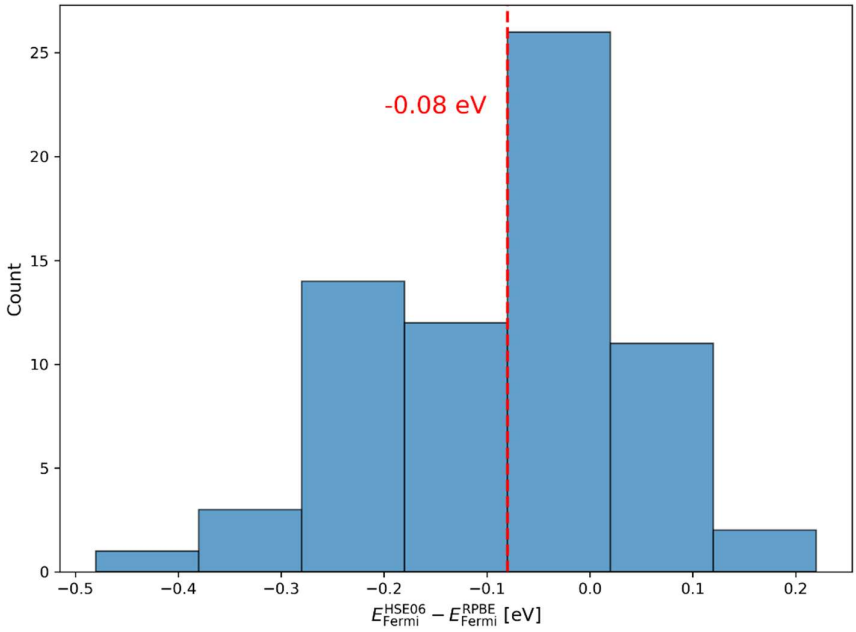

Fig. S9 E_{Fermi} (as defined in eqn (7)) difference between HSE06 and RPBE. The bin size is equal to 0.1 eV. The red dashed line corresponds to the mean of the distribution.

Section S6: Trends in ΔG_{*O} and E_{Fermi} by guest variation on each host composition

The variation of the guest element on each pure oxide host composition (Fig. S10) reveals correlation between $\Delta G_{*\mathrm{O}}$ and E_{Fermi} in the data where the semiconducting TiO_2 and SnO_2 are the hosts (Fig. S10a and b). This is attributed to the influence of the guest d states on the band gap of the host, determining the E_{Fermi} position. The points that correspond to Ti, Sn, and Zr guests in TiO_2 and SnO_2 hosts do not follow this trend because they do not produce any states in the band gap of the host. For the rest of the host ensembles (Fig. S10c-h), the guests do not perturb the E_{Fermi} due to the conducting nature of the hosts.

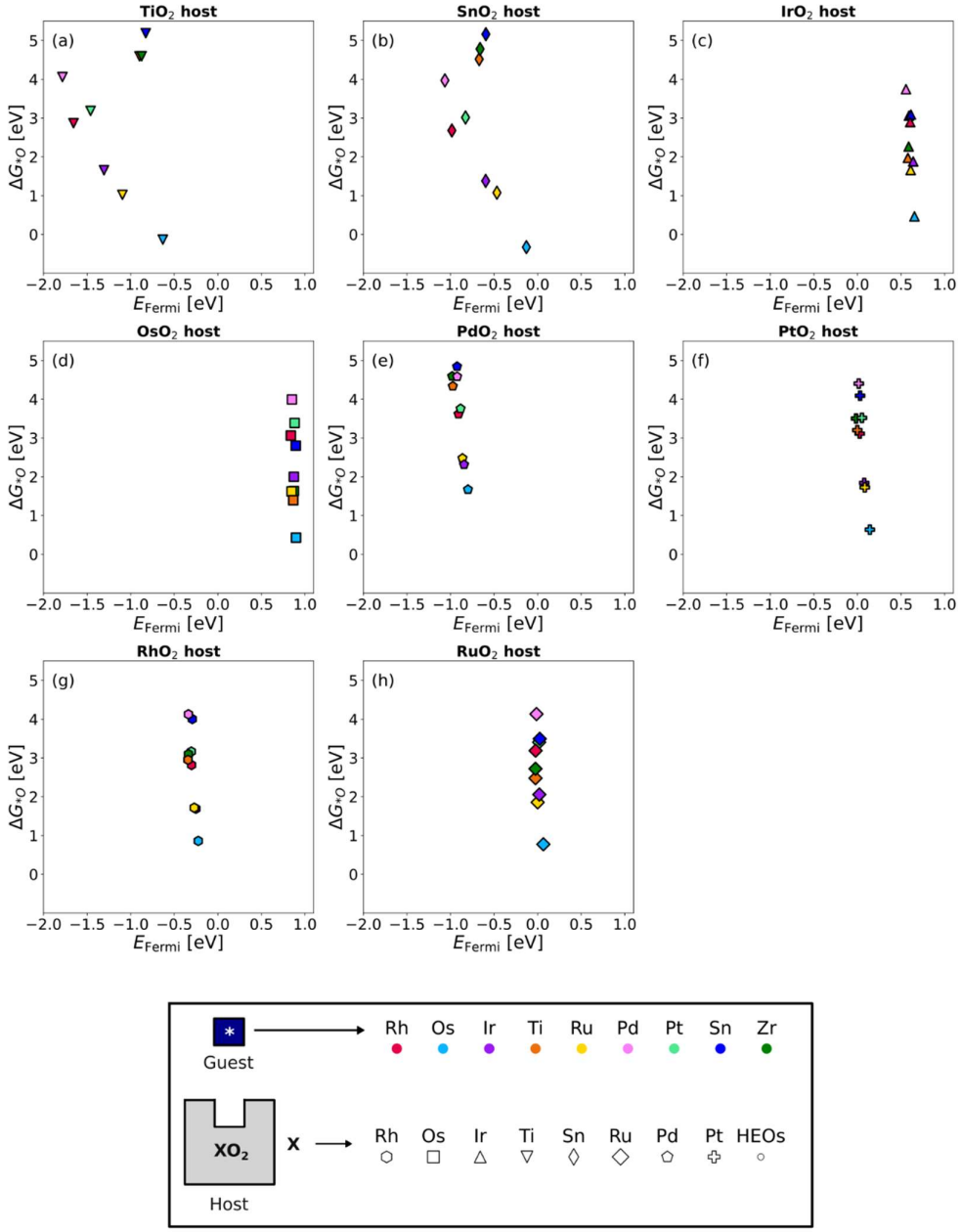

Fig. S10 Correlation between the $\Delta G_{*\mathrm{O}}$ and the E_{Fermi} as the guest element is varied for each pure-host composition. Markers represent different host compositions and colours correspond to different guest elements, as described in the legend.

Section S7: Scaling between the adsorption energies of *O and *OH

To derive the scaling relation, we performed a linear fit between $\Delta G_{*\mathrm{O}}$ and $\Delta G_{*\mathrm{OH}}$ (Fig. S11). We excluded data where TiO_2 and SnO_2 are the host composition from the fits, because they have adsorption energies that deviate from the general trend, due to their semiconducting nature.

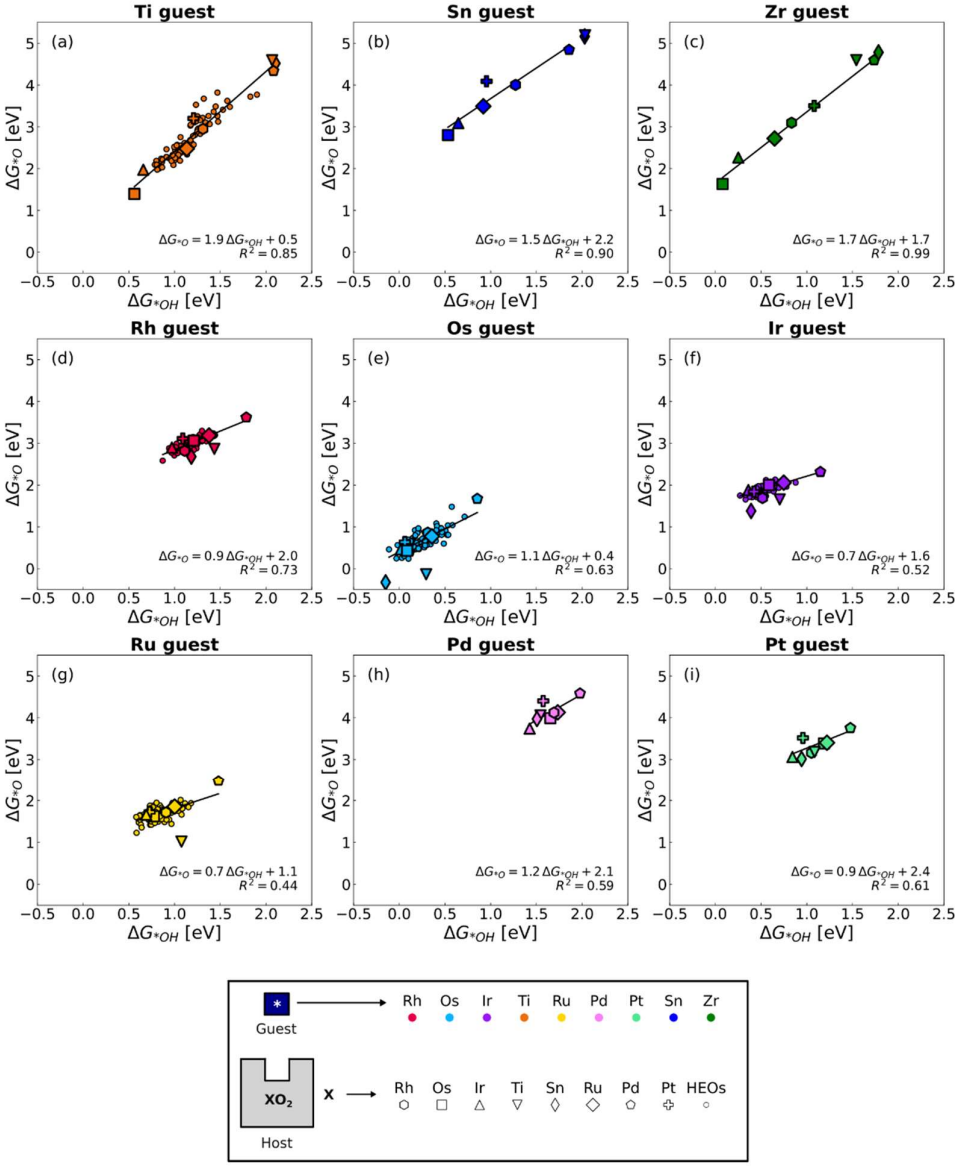

Fig. S11 Scaling relations between the adsorption free energies of *OH and *O, $\Delta G_{*\mathrm{O}} = a\Delta G_{*\mathrm{OH}} + b$, where a is the slope and b is the intercept, for each of the guest elements under study. The markers represent different host compositions and colours correspond to different guest elements, as described in the legend.

Section S8: Bader charge differences in pure oxide hosts

Fig. S12 shows the Bader[13] charge difference at the adsorption site for the different combinations of guest elements and pure oxide hosts. The data follows the trends expected from the HEOs data (Fig. 3a and 3b); a change in Bader charge of the adsorption site atom upon adsorption of *OH ($\Delta q_{*\mathrm{OH}}$) and *O ($\Delta q_{*\mathrm{O}}$) is observed for the elements that can access higher oxidation states than 4+, while for Ti, Sn and Zr the change in the charge is close to 0. The only exceptions to this trend are the Sn sites in OsO_2 and IrO_2 hosts, which still exhibit a significant change difference. This could be related to a change in the oxidation state of Sn, upon incorporation in OsO_2 and IrO_2 hosts, e.g. that Sn changes to 2+ while some nearby Os atoms increase their oxidation state.

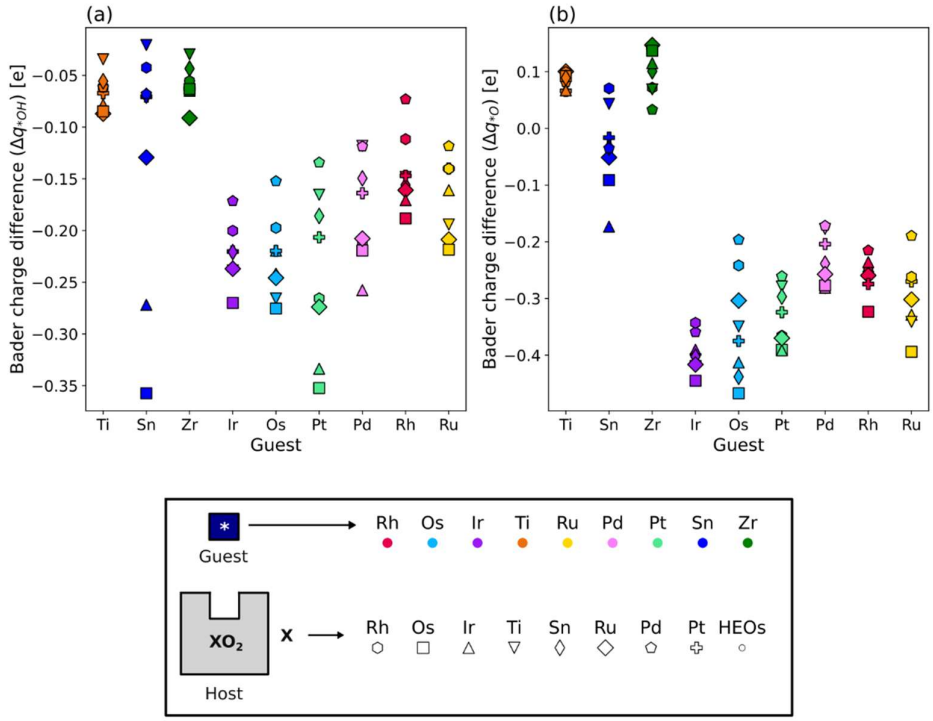

Fig. S12 Bader charge difference ($\Delta q_{*\mathrm{A}}$) at the adsorption site atom in the data where the host composition is a pure oxide after (a) *OH and (b) *O adsorption.

Section S9: Change in distance between adsorption site and oxygen atom beneath

Fig. S13 shows the change in the distance between the adsorption site atom and the oxygen atom beneath it, upon adsorption of *OH ($\Delta d_{*\mathrm{OH}}$) and *O ($\Delta d_{*\mathrm{O}}$) for the different combinations of guest elements and pure oxide hosts. The data follows the trends expected from the HEOs data (Fig. 3c and 3d); a large displacement upon adsorption of *OH and *O is observed for the elements that cannot access higher oxidation states than 4+, i.e. Ti, Sn and Zr, while only small changes are observed for the elements that can access higher oxidation states. A few points behave slightly differently than expected, namely some Pt and Pd adsorption sites which in some cases exhibit negative displacements. Moreover, some Sn sites exhibit only minor displacements, and the underlying cause remains unclear.

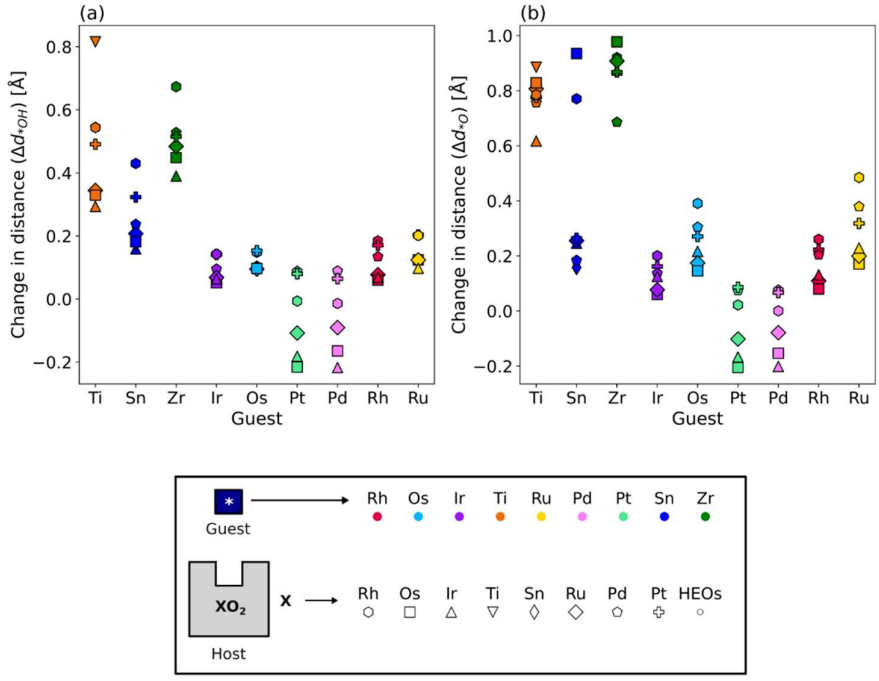

Fig. S13 Change in the distance ($\Delta d_{*\mathrm{A}}$) between the adsorption site atom and the oxygen atom directly beneath it after (a) *OH and (b) *O adsorption.

Section S10: Scaling relation between *OH and *OOH for Ti guest sites

Fig. S14 and Table S5 demonstrate the scaling relations obtained for the adsorbates on the Ti guest sites of the HEOs data. Notably, the *OH intermediate is consistently more thermodynamically stable than the *O + Hb, with only a few exceptions (Fig. S14a). When comparing the energies of the three possible intermediates of the third step of the OER, it becomes evident that O_2(g) + Hb and $*O_2$ + Hb are generally more favorable pathways than *OOH (Fig. S14b), enabling activities beyond the limitations of the conventional volcano (Fig. S14c). This is related to the absence of linear scaling with the adsorption free energies of *OH, in contrast to *OOH intermediate, which exhibits a moderate correlation with *OH (see Table S5). As a result, these data points deviate from the expected volcano trend. Conversely, in the few cases where *OOH is the most stable intermediate, the less favorable scaling with *OH leads to higher overpotentials. This has also previously been observed on doped TiO_2.[14]

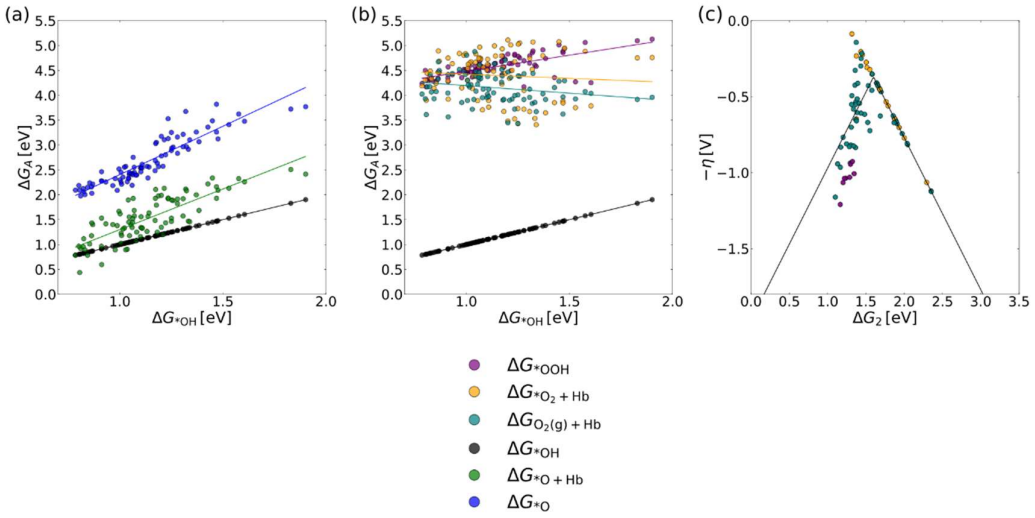

Fig. S14 Scaling relations between the adsorption free energy of *OH with those of (a)*O+Hb, and *O, and those of (b) *OOH , $*O_2$ + Hb and O_2(g)+Hb on Ti guest sites of the HEOs data. Black points in (a) and (b) show *OH vs *OH (self-scaling) for reference. The lines indicate the best linear fits. (c) Negative theoretical overpotentials ($-\eta$) of the Ti sites as a function of the free energy of the second catalytic step (ΔG_2) of the OER. Points are colored by the most stable intermediate in the third step of the OER (*OOH, $*O_2$ + Hb, or O_2(g)+Hb). The volcano plot line is generated by employing the known scaling relation of $\Delta G_{*\mathrm{OOH}} \approx \Delta G_{*\mathrm{OH}} + 3.2$ eV.

Table S5 Equations of the scaling relations between the adsorption free energy of *OH with those of *O+Hb, *O, *OOH, $*O_2$ + Hb and O_2(g)+Hb on Ti guest sites of the HEOs data.

Scaling relation	R^2
$\Delta G_{*O+Hb} = 1.63\Delta G_{*OH} - 0.33$	0.66
$\Delta G_{*O} = 1.94\Delta G_{*OH} + 0.46$	0.83
$\Delta G_{*OOH} = 0.65\Delta G_{*OH} + 3.83$	0.48
$\Delta G_{*O2+Hb} = -0.17\Delta G_{*OH} + 4.59$	0.01
$\Delta G_{O2(g)+Hb} = -0.30\Delta G_{*OH} + 4.50$	0.05

Section S11: Scaling relations and conventional volcano plots for the TiO_2-coated metal (Ru, Rh, Ir, Os, Pd, Pt) oxides

Fig. S15 shows the scaling relations between *OH and each of *OOH, $*O_2$ + Hb, and O_2(g) + Hb (see the resulting scaling relation equations in Table S6) of the TiO_2-coated metal (Ru, Rh, Ir, Os, Pd, Pt) oxides with one TiO_2 overlayer, along with the theoretical overpotentials (η) as a function of the free energy of the second catalytic step (ΔG_2) of the OER. The systems that exceed the volcano prefer the O_2(g) + Hb pathway, due to the lack of scaling with *OH, as also observed for the single Ti sites data. The systems that prefer the *OOH pathway have lower activity than expected from the volcano trend due to less favourable scaling between *OH and *OOH.

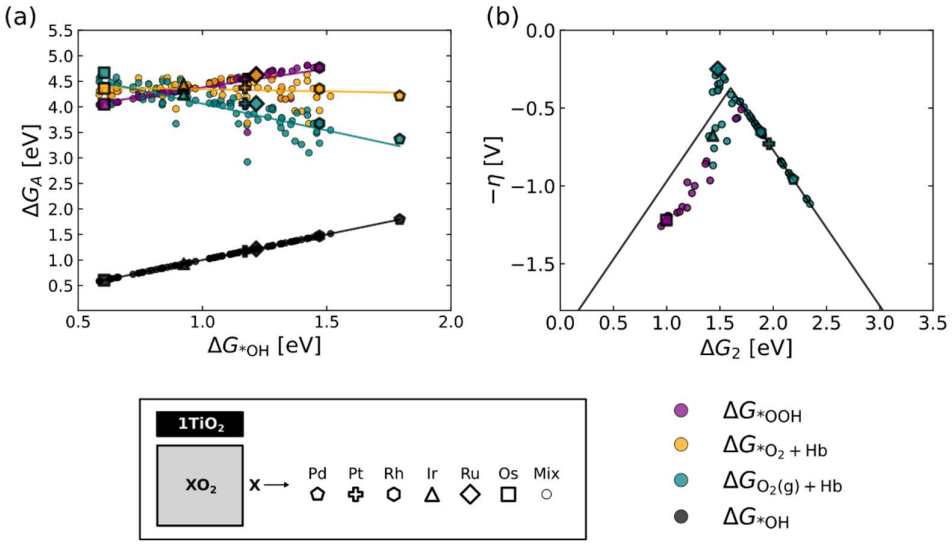

Fig. S15 (a) Scaling relations between the adsorption free energy of *OH with those of *OOH, $*O_2$ + Hb and O_2(g)+Hb on the TiO_2 coated oxides with one TiO_2 overlayer. Black points show *OH vs *OH (self-scaling) for reference. The lines indicate the best linear fits. (b) Conventional volcano plots of the TiO_2 coated oxides data. The volcano plot line is generated by employing the known scaling relation of $\Delta G_{*\mathrm{OOH}} \approx \Delta G_{*\mathrm{OH}} + 3.2$ eV.

Table S6 Equations of the scaling relations between the adsorption free energy of *OH with those of *OOH, $*O_2$ + Hb and O_2(g)+Hb on the TiO_2 coated oxides covered with one TiO_2 overlayer.

Scaling relation	R^2
$\Delta G_{*OOH} = 0.74\Delta G_{*OH} + 3.66$	0.56
$\Delta G_{*O2+Hb} = -0.08\Delta G_{*OH} + 4.49$	0.01
$\Delta G_{O2(g)+Hb} = -1.05\Delta G_{*OH} + 5.23$	0.66

Section S12: D3-corrections

To investigate the effect of van der Waals interactions on our systems, we added the D3-correction[15] to our RPBE calculations for all TiO_2-coated metal oxides (Ru, Rh, Ir, Os, Pd, Pt) (single TiO_2 overlayer). As shown in Fig. S16, the RPBE-D3 results yield a roughly constant shift of 0.25 eV in ΔG_2 relative to RPBE, while the trend with E_{Fermi} is essentially unchanged.

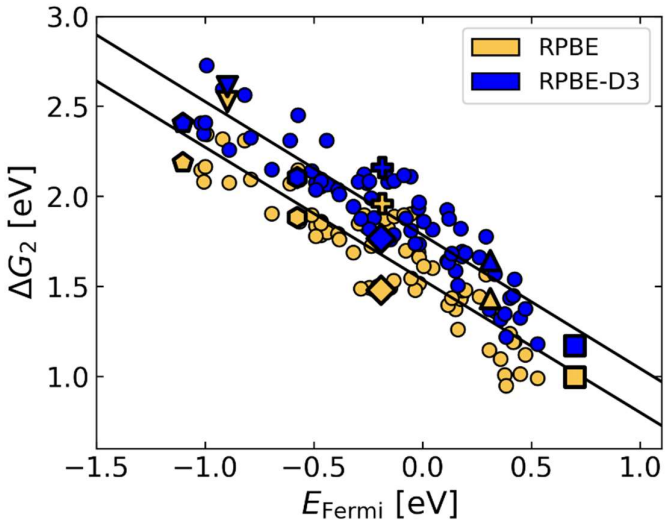

Fig. S16 Correlation between E_{Fermi} and ΔG_2 for the TiO_2-coated metal oxides (M = Ru, Rh, Ir, Os, Pd, Pt) dataset (single TiO_2 overlayer) with RPBE (yellow) and RPBE with D3 corrections (blue). Black lines correspond to the best linear fits.

References

1. I. C. Man, H. Y. Su, F. Calle-Vallejo, H. A. Hansen, J. I. Martínez, N. G. Inoglu, J. Kitchin, T. F. Jaramillo, J. K. Nørskov and J. Rossmeisl, *ChemCatChem*, 2011, **3**, 1159-1165.
2. K. L. Svane, *Curr. Opin. Electrochem.*, 2025, **51**.
3. N. B. Halck, V. Petrykin, P. Krtil and J. Rossmeisl, *Phys. Chem. Chem. Phys.*, 2014, **16**, 13682-13688.
4. A. Hjorth Larsen, J. Jorgen Mortensen, J. Blomqvist, I. E. Castelli, R. Christensen, M. Dulak, J. Friis, M. N. Groves, B. Hammer, C. Hargus, E. D. Hermes, P. C. Jennings, P. Bjerre Jensen, J. Kermode, J. R. Kitchin, E. Leonhard Kolsbjerg, J. Kubal, K. Kaasbjerg, S. Lysgaard, J. Bergmann Maronsson, T. Maxson, T. Olsen, L. Pastewka, A. Peterson, C. Rostgaard, J. Schiotz, O. Schutt, M. Strange, K. S. Thygesen, T. Vegge, L. Vilhelmsen, M. Walter, Z. Zeng and K. W. Jacobsen, *J. Phys. Condens. Matter*, 2017, **29**, 273002.
5. J. Enkovaara, C. Rostgaard, J. J. Mortensen, J. Chen, M. Dulak, L. Ferrighi, J. Gavnholt, C. Glinsvad, V. Haikola, H. A. Hansen, H. H. Kristoffersen, M. Kuisma, A. H. Larsen, L. Lehtovaara, M. Ljungberg, O. Lopez-Acevedo, P. G. Moses, J. Ojanen, T. Olsen, V. Petzold, N. A. Romero, J. Stausholm-Moller, M. Strange, G. A. Tritsaris, M. Vanin, M. Walter, B. Hammer, H. Hakkinen, G. K. Madsen, R. M. Nieminen, J. K. Norskov, M. Puska, T. T. Rantala, J. Schiotz, K. S. Thygesen and K. W. Jacobsen, *J. Phys.: Condens. Matter*, 2010, **22**, 253202.
6. J. J. Mortensen, L. B. Hansen and K. W. Jacobsen, *Phys. Rev. B*, 2005, **71**.
7. B. Hammer, L. B. Hansen and J. K. Nørskov, *Phys. Rev. B*, 1999, **59**, 7413-7421.
8. K. L. Svane and J. Rossmeisl, *Angew. Chem.*, 2022, **61**, e202201146.
9. S. Divanis, T. Kutlusoy, I. M. Ingmer Boye, I. C. Man and J. Rossmeisl, *Chem. Sci.*, 2020, **11**, 2943-2950.
10. H. P. R. Frederikse, *J. Appl. Phys.*, 1961, **32**, 2211-2215.
11. K. Reimann and M. Steube, *Solid State Commun.*, 1998, **105**, 649-652.
12. J. Heyd, G. E. Scuseria and M. Ernzerhof, *J. Chem. Phys.*, 2003, **118**, 8207-8215.
13. G. Henkelman, A. Arnaldsson and H. Jónsson, *Comput. Mater. Sci.*, 2006, **36**, 354-360.
14. N. Govindarajan, J. M. García-Lastra, E. J. Meijer and F. Calle-Vallejo, *Curr. Opin. Electrochem.*, 2018, **8**, 110-117.
15. S. Grimme, J. Antony, S. Ehrlich and H. Krieg, *J. Chem. Phys.*, 2010, **132**.